J Mater Sci (2010) 45:1595–1603
DOI 10.1007/s10853-009-4130-3

Synthesis, characterization, and evaluation of lubrication properties of composites of ordered mesoporous carbons and luminescent $CePO_4$:Tb nanocrystals

Falk Heinroth · Dominic Gruss · Sven Müller · Florian Waltz · Julia Martynczuk · Armin Feldhoff · Peter Behrens · Michael Wiebcke

Received: 30 August 2009 / Accepted: 14 December 2009 / Published online: 29 December 2009

Abstract Having new potential applications in forging processes in mind, composites of an ordered mesoporous carbon and luminescent metal phosphate nanocrystals were synthesized for the first time. Three kinds of CMK-3/$CePO_4$:Tb nanocomposites were prepared by treating a mesoporous CMK-3 host with different lanthanide phosphate precursor solutions. Characterization of the obtained nanocomposites by small-angle X-ray scattering, wide-angle X-ray diffraction, transmission electron microscopy, thermogravimetry, and nitrogen physisorption analysis showed that in two cases, the nanocrystals (ca. 2–3 nm in size) were located inside the mesopores, whereas in the third case the nanocystals (ca. 6 nm in size) merely adhered to the outer surfaces of the carbon particles. The CMK-3 and the two nanocomposites had ordered hexagonal structures (space group *p6mm*); all the materials possessed amorphous carbon walls. After combustion of the nanocomposites, the residues upon excitation with UV light exhibited the typical green luminescence of Tb^{3+}. A preliminary evaluation of the lubrication properties of the CMK-3 and one nanocomposite material was performed. The friction factors determined by means of ring upsetting tests revealed that the carbon materials were able to lower frictional forces although they were 3–4 times less efficient than a commercial graphite-based reference lubricant.

F. Heinroth · F. Waltz · P. Behrens · M. Wiebcke (✉)
Institut für Anorganische Chemie, Leibniz Universität Hannover, Callinstr. 9, 30167 Hannover, Germany
e-mail: michael.wiebcke@acb.uni-hannover.de

D. Gruss · S. Müller
Institut für Integrierte Produktion gGmbH, Holleritallee 6, 30419 Hannover, Germany

J. Martynczuk · A. Feldhoff
Institut für Physikalische Chemie und Elektrochemie, Leibniz Universität Hannover, Callinstr. 3A, 30167 Hannover, Germany

F. Heinroth · F. Waltz · A. Feldhoff · P. Behrens · M. Wiebcke
Zentrum für Festkörperchemie und Neue Materialien, Leibniz Universität Hannover, Callinstr. 3A, 30167 Hannover, Germany

Present Address:
J. Martynczuk
Nichtmetallische Anorganische Werkstoffe, ETH Zürich, Wolfgang-Pauli-Str. 10, CH-8093 Zürich, Switzerland

Introduction

Ordered mesoporous carbons (OMCs) have attracted a great deal of attention due to their numerous potential applications such as catalysts, separation media, and advanced electronic materials [1–6]. We became interested in OMCs considering the problems in current massive forming processes such as forging processes. Owing to the strong frictional forces that occur between workpiece and tool, a lubricant has to be applied to minimize abrasive wear as well as energy consumption. Further problems concern the decarburization of surface layers in the case of steel, the formation of scale layers (i.e., oxidative corrosion), as well as the formation of cracks and folds. It appeared to us that OMCs have the potential as basis materials for the development of advanced lubrication systems that, in combining different functions, could serve to solve some of the mentioned problems simultaneously, and thereby lead to a shortening of current forging process chains. For example, the carbon walls of OMC particles, which are usually amorphous in as-synthesized OMCs, can be graphitized by proper choice of carbon precursors and annealing at high temperatures [7–11]. This could render OMCs good lubricants. As a reductant, carbon could

suppress the formation of scale. Furthermore, functional species such as nanoparticles can be inserted into the mesopore systems or incorporated in the carbon walls giving rise to functional OMC nanocomposites [12–18]. For example, thermally stable fluorescent inorganic nanoparticles which are contained in an OMC could be distributed preferentially in microcracks generated in a workpiece or tool during a forging process, and thereby help to easily detect such microcracks directly after the process simply by irradiating the workpiece or tool with UV light. This becomes possible because the nontransparent carbon matrix is usually burnt at the high temperatures of forging processes. Further advantages of OMCs are the many different pore morphologies that can be obtained and the possibility of tuning pore size as well as particle size. With these ideas in mind, we recently started a joint project consisting of materials' chemists and engineers, which aims at developing advanced OMC-based lubrication systems.

The most investigated OMC is probably that of the CMK-3, the carbon host structure of which consists of a hexagonal array of parallel nanorods that are interconnected by smaller bridges (negative replica structure of mesoporous silica SBA-15) [7–10, 13, 15–17, 19–23]. This carbon material was chosen to prepare composites of CMK-3 and fluorescent Tb-doped $CePO_4$ nanocrystals, which were characterized by small-angle X-ray scattering (SAXS), wide-angle X-ray diffraction (XRD), transmission electron microscopy (TEM), thermogravimetric (TG) analysis, nitrogen physisorption measurements, and photoluminescence (PL) spectroscopy. The experiments and results are reported here. In addition, we report on a preliminary evaluation of the lubrication properties of CMK-3 and one of the prepared nanocomposites by means of ring upsetting tests. To the best of our knowledge, so far there have been no reports on OMC-metal phosphate nanocomposites, and on lubrication properties of OMC-based materials.

Experimental section

All reagents were commercially purchased and used as received. CMK-3 was prepared via the nanocasting route using a mesoporous silica SBA-15 as an exotemplate and sucrose as the carbon source according to literature protocols [19]. For the preparation of CMK-3/$CePO_4$:Tb nanocomposites, three different kinds of lanthanide phosphate precursor solutions were used for infiltration of CMK-3. The chemical compositions of the precursor solutions and the conditions of nanocomposite syntheses were adopted with modification from literature protocols for the syntheses of pure $CePO_4$:Tb nanocrystals.

Synthesis of CMK-3/$CePO_4$:Tb nanocomposites from diphenylether precursor solutions (NC-DPE)

The protocol was adopted with modification from the studies of Haase and co-workers on pure nanocrystals [24, 25]. 5.58 g (15 mmol) of $CeCl_3 \cdot 7H_2O$ and 1.85 g (5 mmol) of $TbCl_3 \cdot 6H_2O$ were dissolved in 20 mL of methanol. To the clear solution, 21.6 mL of tributylphosphate was added, and methanol was removed using a rotary evaporator. Then, 60 mL of diphenylether (DPE) was added, and water was evacuated with the help of an oil pump. Then, 10.2 mL of trihexylamine and 7 mL of a 2 M solution of water-free H_3PO_4 dissolved in dihexylether were added. To this precursor solution, 0.3 g of CMK-3 was added. The mixture was ultrasonicated for 15 min and then refluxed at 200°C for 4 h in a constant flow of argon. After cooling to room temperature, the nanocomposite was recovered by filtration, washing with water and ethanol, and air-drying at 50°C for 24 h.

Synthesis of CMK-3/$CePO_4$:Tb nanocomposites from aqueous precursor solutions (NC-W)

The protocol was adopted with modification from the study of Boilot and co-workers [26] on pure nanocrystals. 0.43 g (1 mmol) of $Ce(NO_3)_3 \cdot 6H_2O$ and 0.07 g (0.15 mmol) of $Tb(NO_3)_3 \cdot 6H_2O$ were dissolved in 10 mL of water. In addition, 0.42 g (1.14 mmol) of sodium triphosphate ($Na_5P_3O_{10}$) was dissolved in 10 mL of water. The aqueous solutions were combined, and 0.3 g of CMK-3 was added. The mixture was ultrasonicated for 15 min and then heated to 90°C at reflux for 3 h. After cooling to room temperature, the mixture was dialyzed for 24 h against deionized water. Then, 2 mL of a 0.1 M aqueous solution of sodium metahexaphosphate [$(NaPO_3)_{12-13} \cdot Na_2O$] was added, and the mixture was further dialyzed for 72 h. Finally, the nanocomposite was recovered by filtration, washing with water and ethanol, and air-drying at 50°C for 24 h.

Synthesis of CMK-3/$CePO_4$:Tb nanocomposites from diethyleneglycol precursor solutions (NC-DEG)

The protocol was adopted with modification from the studies of Feldmann and Jungk [27, 28] and Feldmann [27, 28] on pure nanocrystals. 0.83 g (22 mmol) of $CeCl_3 \cdot 7H_2O$ and 0.27 g (0.7 mmol) of $TbCl_3 \cdot 6H_2O$ were dissolved in 50 mL of diethyleneglycol (DEG), and 0.3 g of CMK-3 was added. The mixture was heated to 100 °C in a constant flow of argon. Then, 0.41 g (40 mmol) of water-free H_3PO_4 dissolved in 10 mL of DEG and 3 mL of trihexylamine were added. The resulting mixture was heated under argon to 180 °C at reflux for 5 min and then cooled to room temperature. The nanocomposite was recovered by

filtration, washing with water and ethanol, and air-drying at 50 °C for 24 h.

Methods of characterization

Powder XRD patterns were recorded at room temperature on a Stoe STADI P diffractometer in transmission mode on flat samples using Ge(111)-monochromatized $CuK_{\alpha 1}$ radiation of wavelength 0.1540598 nm. The diffractometer was equipped with a small linear position-sensitive detector. The Scherrer equation was applied to estimate nanocrystal sizes from the broadening of XRD peaks. For taking powder patterns at low angles, a Rigaku SAXS instrument was employed. This instrument was equipped with a Bede X-ray microsource, Osmic mirror optics, three pin holes, and a 2D gas-filled multiwire detector. The measurements were performed in transmission mode at room temperature using CuK_{α} radiation of wavelength 0.154 nm. A silver behenate sample was used to calibrate the sample-to-detector distance. The scattering patterns were azimuthally averaged to obtain the 1D scattering patterns.

A Jeol JEM-2100F-UHR field-emission instrument equipped with a Gatan GIF 2001 energy filter and a 1k-CCD camera operating at 200 kV was used to take TEM images. Samples were dispersed on a copper-supported carbon film.

Thermogravimetric analysis was performed on a Netzsch 429 Thermoanalyser. For this purpose, ca. 30 mg of material was filled into alumina crucibles and heated in a flow of air with a ramp of 5 °C min^{-1} up to 1,000 °C. Nitrogen physisorption measurements were performed at −196 °C on a Quantachrome Autosorb-1 volumetric apparatus. Samples were filled into glass tubes and outgassed in vacuum ($\sim 10^{-4}$ mbar) at 200 °C before the sorption measurements. Specific surface areas were determined by applying the Brunauer–Emmett–Teller (BET) equation. Total pore volumes were estimated by the single-point method (at $p/p_0 \approx 0.98$). Non-local density functional theory (NLDFT) was applied to estimate pore-size distributions (kernel for carbon with cylindrical pores, Quatachrome).

Photoluminescence spectra were recorded from powder samples on a Perkin Elmer LS 50 B spectrometer equipped with a Xe lamp.

Ring upsetting tests

In the field of massive forming, the ring upsetting test is a widely accepted method to determine key figures of friction, for example, the dimensionless friction factor, m [29, 30]. In ring upsetting tests, a flat ring specimen is plastically compressed between two coplanar upsetting plates. From the change of the geometrical dimensions of the compressed ring, the friction factor, m, can be determined [29, 30]. At a height reduction of 50%, an approximate value of m can be obtained from the reduced inner diameter d_{iRed} (difference between inner diameter d_i before and after compression) by

$$m \approx 0.1671 \cdot \exp(0.04 \cdot d_{iRed}).$$

The ring specimen used here was made of a non-alloy carbon steel (C45N, workpiece number 1.1730) and had the following dimensions: outer diameter, 30 mm; inner diameter, 15 mm; and height, 10 mm. The specimen was heated in a furnace coated with the lubricant to 750 °C, and then quickly mounted on a percussion press (type PSR 160, Weingarten, maximum force 2,500 kN, or type PSH 4.265f, Müller–Weingarten, maximum force 7,000 kN) to perform the test. The lubricant Lubrodal 25 PLE (graphite:water = 1:10) was purchased from Fuchs Lubritech and used as a reference.

Results and discussion

Synthesis and characterization of CMK-3/$CePO_4$:Tb nanocomposites

The CMK-3, used as the host for the syntheses of the nanocomposites, was prepared by nanocasting a silica SBA-15 exotemplate according to literature protocols [19], and had a well-ordered hexagonal structure. In brief, the ordered structure was evidenced by TEM images (Fig. 1a) and the SAXS pattern, which showed three clearly resolved peaks, which were indexed in the 2D space group *p6mm* (lattice constant $a = 9.9$ nm). Comparison of the SAXS pattern of the CMK-3 (Fig. 2b) with the pattern taken from the SBA-15 exotemplate (Fig. 2a) reveals that the ordered structure of the SBA-15 had been well casted. The absence of any peak in the XRD pattern (Fig. 3a) demonstrated that the carbon walls were amorphous. According to TG, the CMK-3 was thermally stable in air up to ca. 400 °C, and the low residual mass (2%) obtained after TG indicated that leaching of the initial silica mold was nearly complete. A specific surface area of 1,580 m^2 g^{-1} and a total (micro- and mesopore) volume of 1.25 cm^3 g^{-1} were estimated from the adsorption branch of the type IV nitrogen sorption isotherms (Fig. 4a). The mesopores had a size distribution between 3 and 5 nm (Fig. 5a). All these data, when compared with previous reports [19], demonstrated the high quality of the CMK-3.

Three kinds of composites of CMK-3 and $CePO_4$:Tb nanocrystals were prepared by treating the CMK-3 with different lanthanide phosphate precursor solutions that were based, respectively, on DPE, water (W), and diethyleneglycol (DEG) as the solvent (see "Experimental

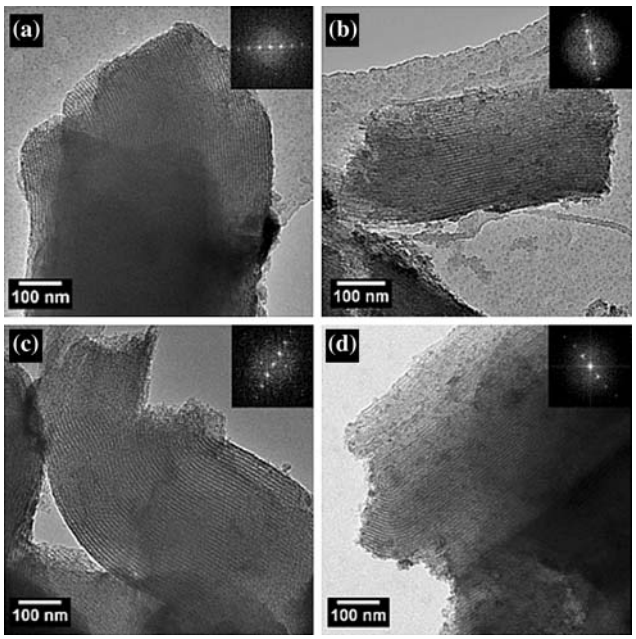

Fig. 1 TEM images of **a** CMK-3, **b** NC-DPE, **c** NC-W, and **d** NC-DEG. Fourier transforms of the patterns are shown in the *insets*

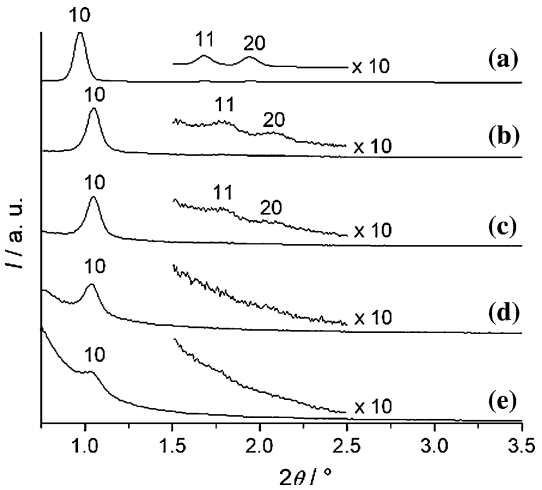

Fig. 2 SAXS patterns of (*a*) SBA-15 exotemplate, (*b*) CMK-3, (*c*) NC-DPE, (*d*) NC-W, and (*e*) NC-DEG. Indices correspond to the hexagonal space group *p6mm*

section"). The chemical compositions of the precursor solutions as well as the conditions of nanocomposite syntheses were adopted with slight modifications from literature protocols for the syntheses of pure Tb-doped lanthanide phosphate nanocrystals [24–28]. It should be noted that the procedures used here for nanocomposite synthesis differed from the common wet-chemical methods of nanoparticle synthesis and stabilization in mesoporous materials, namely, wet impregnation or incipient wetness [31]. Both methods usually involve a drying step after pore infiltration by the precursor solution before nanoparticle formation is initiated. An intermediate drying step was not performed here. Hereafter, the nanocomposites obtained are denoted NC-DPE, NC-W, and NC-DEG. The results are presented in the respective order.

NC-DPE

A TEM image (Fig. 1b) and the SAXS pattern (Fig. 2c) of the obtained NC-DPE demonstrate that the carbon host structure had survived the synthesis procedure. The SAXS pattern shows three peaks that are compatible with space group *p6mm* (lattice constant $a = 9.7$ nm). When the SAXS pattern is compared with that of the pure CMK-3 host (Fig. 2b), it can be seen that the relative intensities of the three peaks are different in both patterns; the ratios I_{10}/I_{11} and I_{10}/I_{20} are larger for NC-DPE than for the pure CMK-3. This can be explained by a change in the electron-density contrast (chemical composition) between walls and pores and suggests that loading of pores had occurred. The XRD pattern (Fig. 3b) clearly exhibits weak, broad peaks which resemble the XRD pattern of monoclinic $CePO_4$ (monazite structure type), as already reported by Haase and co-workers for the original nanocrystal synthesis in the absence of CMK-3 [24, 25]. A size of ca. 3 nm was estimated here for the nanocrystals from the broadening of the diffraction peaks, revealing that they were of the correct size to occupy the mesopores of the CMK-3. The distribution of the nanocrystals within the NC-DPE material, whether inside the pores and/or on the outer surfaces of the particles, shall be dealt with further below.

Considering first the TG curve (Fig. 6a), three mass losses are seen that were assigned, respectively, to the evaporation of water being adsorbed on the outer surfaces (1%), the escape of high-boiling components (in particular DPE) from the pores (8%), and removal of the carbon host by combustion (73%). The solid residue obtained after TG (18%) was identified by XRD as monoclinic $CePO_4$ (Fig. 6b). Furthermore, upon excitation with UV light, the residue exhibited a strong green luminescence that is typical for Tb^{3+}. Indeed, Tb-doping of the $CePO_4$ nanocrystals was confirmed by the PL spectrum taken from the residue (Fig. 7). The spectrum consists of emission bands that are apparently exclusively caused by 5*d*–4*f* electronic transitions of Tb^{3+} [32, 33]. The fact that emission bands of Ce^{3+} (typically a broad band between ca. 300 and 400 nm [32]) apparently do not appear in the spectrum further suggests that the short-range energy transfer from Ce^{3+} to Tb^{3+} was efficient, and thus that the degree of Tb-doping of the nanocrystals was rather high. The observation that the NC-DPE material itself upon excitation with UV light was not fluorescent may be taken as a hint that most nanocrystals were located inside the pores.

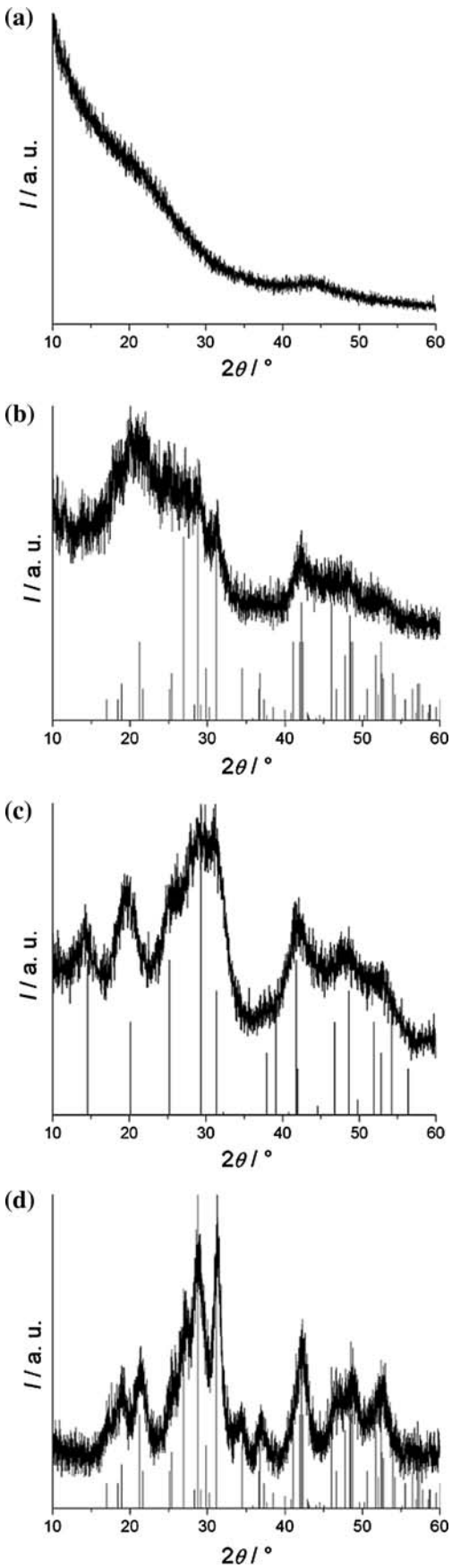

Fig. 3 Experimental powder XRD profiles of **a** CMK-3, **b** NC-DPE, ▶ **c** NC-W, and **d** NC-DEG. Patterns of references are represented as line diagrams: **b**, **d** PDF card 32-199 (monazite), **c** PDF card 4-632 (rhabdophane)

A common method to prove the insertion of guest species into mesopores is by means of gas sorption analysis (reduction of specific internal surface area) [17]. Indeed, a strongly reduced specific surface area of 900 $m^2\ g^{-1}$ was determined from the type IV nitrogen sorption isotherms of NC-DPE (Fig. 4b). The remaining mesopores had sizes between 3 and 5 nm (Fig. 5b). The reduction in surface area can, however, at most only partly be ascribed to loading of the pores with nanocrystals due to the rather high amount of high-boiling components (detected by TG) that were apparently tightly fixed inside the pores due to favorable hydrophobic interactions with the carbon walls. The situation could not be improved by extraction procedures such as heating of NC-DPE with ethanol at reflux for 1 week. TG analysis after that procedure (Fig. 6a) revealed that the mass loss ascribed to high-boiling components (8%) had not changed. Only the mass of the solid residue was reduced (11%), suggesting that a fraction of nanocrystals (ca. 1/3, calculated from the different masses of the TG residues before and after extraction) had adhered to the outer surfaces and was removed by the extraction procedure. We thus conclude that most nanocrystals were located inside the mesopores of NC-DPE.

NC-W

A TEM image (Fig. 1c) and the SAXS pattern (Fig. 2d) of NC-W suggest that the nanocomposite possessed a well-ordered CMK-3-like structure. The fact that only one scattering peak is observed by SAXS can be explained by a change in electron-density contrast due to loading of the pores as already discussed above. Indexing of the peak as 10 reflection gave a lattice constant of $a = 9.8$ nm. The weak, broad diffraction peaks of the XRD pattern (Fig. 3c) are compatible with those of hexagonal hydrated $CePO_4{\cdot}xH_2O$ (rhabdophane structure type), in agreement with the study by Buissette et al. [26] for the original nanocrystal synthesis in the absence of CMK-3. The broadening of the diffraction peaks of NC-W corresponds to a nanocrystal size of ca. 2 nm.

The TG curve (Fig. 8a) exhibits three mass losses that were ascribed, respectively, to the evaporation of water from the pores and surfaces of the particles (15%), the escape of water from hydrated $CePO_4{\cdot}xH_2O$ nanocrystals (5%), and the removal of the carbon by combustion (42%). A rather high amount of solid residue (38%) obtained after TG was identified by XRD as monoclinic $CePO_4$ (Fig. 8b). A thermally induced transformation from the rhabdophane-

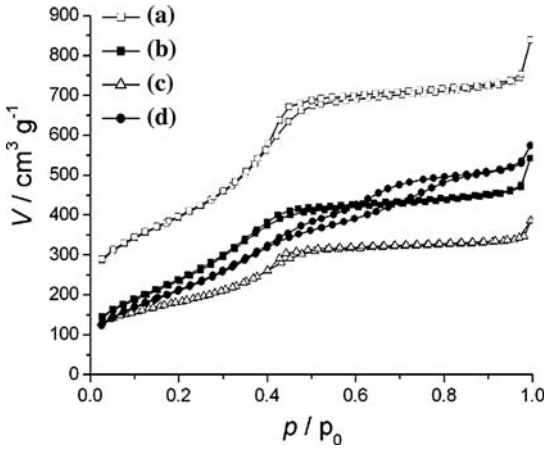

Fig. 4 Nitrogen physisorption isotherms of (*a*) CMK-3, (*b*) NC-DPE, (*c*) NC-W, and (*d*) NC-DEG (measured at −196 °C)

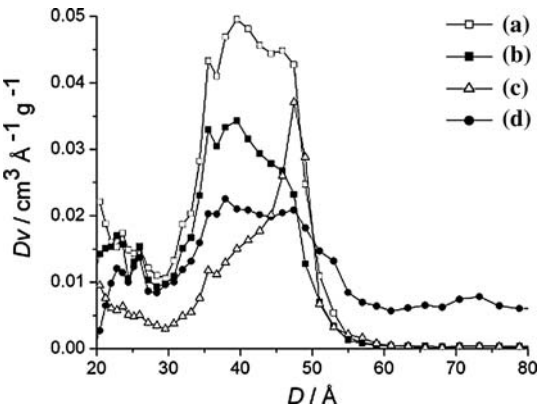

Fig. 5 Mesopore size distributions of (*a*) CMK-3, (*b*) NC-DPE, (*c*) NC-W, and (*d*) NC-DEG (determined from the N_2 sorption data by applying non-local density function theory)

type to the stable monazite-type phase was already observed by Buissette et al. [26] for pure nanocrystals. Upon excitation with UV light, the residue of the TG analysis exhibited the typical green fluorescence of Tb^{3+}. In the PL spectrum (Fig. 9), the emission bands originating from Tb^{3+} are clearly seen. However, the fine structure of the emission bands on the high-energy side at around 400 nm considerably differs from that observed for the nanocrystals obtained after TG of NC-DPE (Fig. 7), and the same might be influenced by emissions of Ce^{3+} [32, 33]. NC-W itself was not fluorescent.

From the type IV nitrogen sorption isotherms (Fig. 4c), a specific surface area of 650 m^2 g^{-1} was determined, which is only 40% of the surface area of the pure CMK-3 host. Since TG had shown that the solvent (water) can be nearly completely removed by heating to 200 °C, in contrast to the situation for NC-DPE, the reduction in surface area can in the case of NC-W be unambiguously attributed

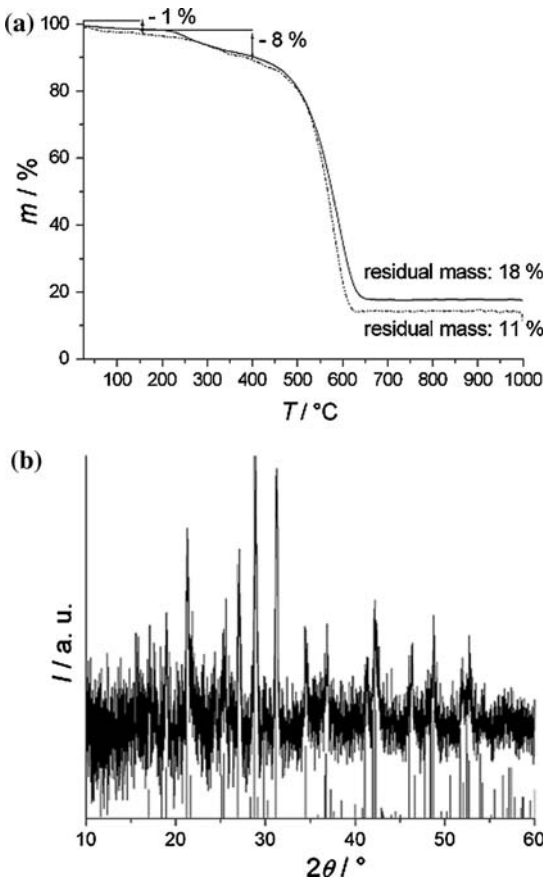

Fig. 6 **a** TG curves of NC-DPE measured before (*solid line*) and after ethanol extraction (*dotted line*) in a flow of air. **b** XRD pattern taken on the residue after TG; a pattern of monazite is represented as line diagram (PDF card 32-199)

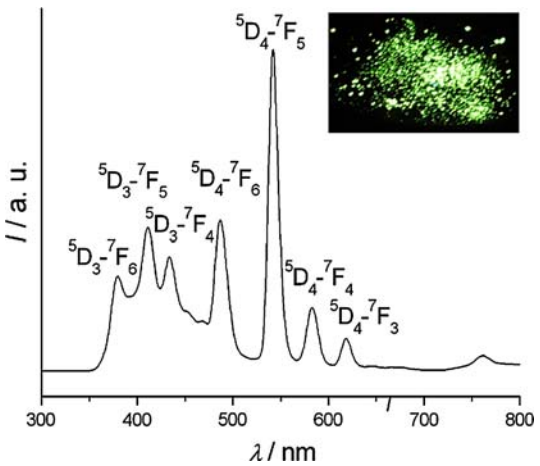

Fig. 7 PL spectrum ($\lambda_{exc} = 270$ nm) of NC-DPE after combustion (TG residue). A photograph taken from the sample while irradiating with UV light is shown in the *inset*

to loading of the pores with nanocrystals. We, thus, conclude that nearly all the nanocrystals were located inside the pores of NC-W.

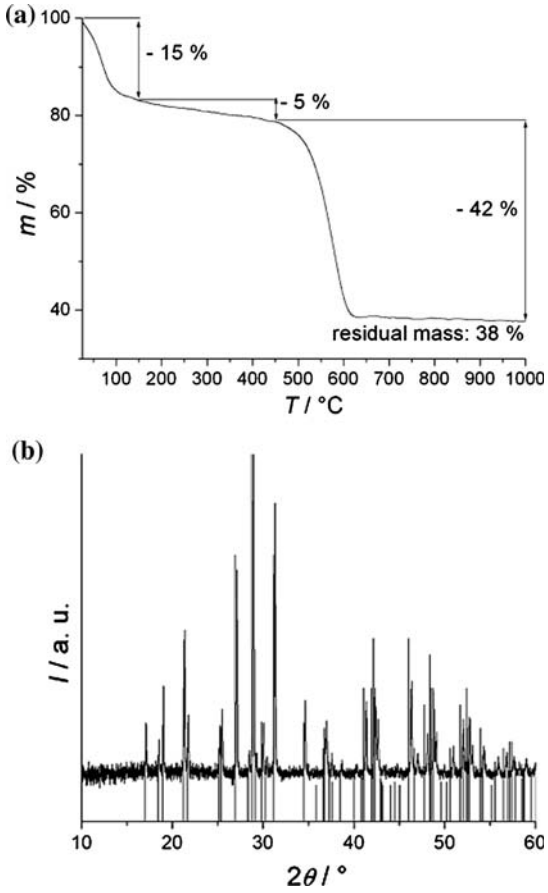

Fig. 8 **a** TG curve of NC-W measured in a flow of air. **b** XRD pattern taken on the residue after TG; a pattern of monazite is represented as line diagram (PDF card 32-199)

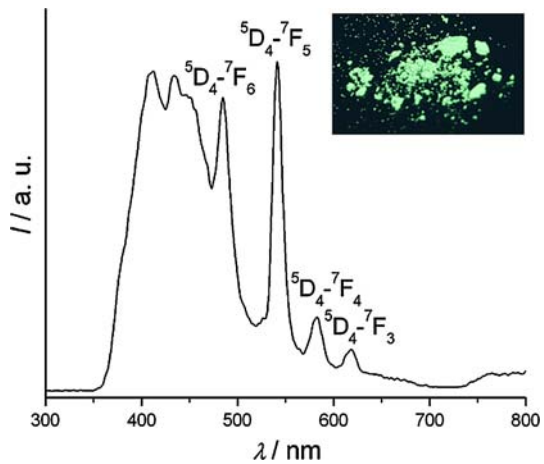

Fig. 9 PL spectrum ($\lambda_{exc} = 270$ nm) of NC-W after combustion (TG residue). A photograph taken from the sample while irradiating with UV light is shown in the *inset*

This is an interesting and a priori unexpected result because water was used as the solvent which should not readily penetrate into the hydrophobic pores of a CMK-3 carbon. For that reason, in previous studies the surfaces of OMCs were either made more hydrophilic (e.g., by treatment with sulfuric acid) before infiltration with aqueous solutions or less polar solvents (e.g., ethanol) was used [16, 17].

NC-DEG

On the TEM image of a NC-DEG particle (Fig. 1d), an ordered array of parallel walls and mesopores can be seen. However, the SAXS pattern (Fig. 2e) exhibits only one broad peak on a high background which rises toward low 2Θ values, and the nitrogen sorption isotherms (Fig. 4d) do not exhibit a well-developed step at medium relative pressure. Thus, both these methods, which are representative of the whole sample, indicate that in the course of nanocomposite synthesis considerable degradation of the CMK-3 structure takes place. The XRD pattern (Fig. 3d) resembles that of monoclinic $CePO_4$, as observed previously for the synthesis of pure nanocrystals in the absence of CMK-3 by Feldmann and Jungk [27] and Feldmann [28]. From the broadening of the diffraction peaks, it was estimated that the nanocrystals had an average size of 6 nm, which is clearly larger than the mesopore diameter of the pure CMK-3 host (<5 nm). Furthermore, upon excitation with UV light, NC-DEG strongly exhibited the green luminescence of Tb^{3+}. On the TG curve (Fig. 10a), three mass losses are seen that were ascribed, respectively, to the escape of water (7%) and high-boiling DEG (7%), respectively, from the pores and surfaces of NC-DEG particles, and the removal of the carbon by combustion (22%). A very high amount of solid residue (64%) obtained after TG was identified by XRD as monoclinic $CePO_4$ (Fig. 10b). The reduced surface area (820 $m^2\ g^{-1}$) determined from the nitrogen sorption isotherms (Fig. 4d) cannot serve as a proof of loading of the mesopores by nanocrystals due to the presence of DEG as detected by TG. The mesopores of NC-DEG had a rather broad size distribution (Fig. 5d). From all the above data, it can be safely concluded that most nanocrystals were not located inside the pores but merely adhered to the surfaces of the NC-DEG particles.

Evaluation of CMK-3 and CMK-3/$CePO_4$:Tb nanocomposites as potential lubricants

In order to gain first insight into the potential of OMCs and OMC/phosphate nanocrystal composites to perform as lubricants in forging applications, we evaluated the lubrication properties of our CMK-3 and NC-DEP materials by means of ring upsetting tests. In the field of massive forming, the ring upsetting test is a widely accepted method to determine key figures of friction, for example,

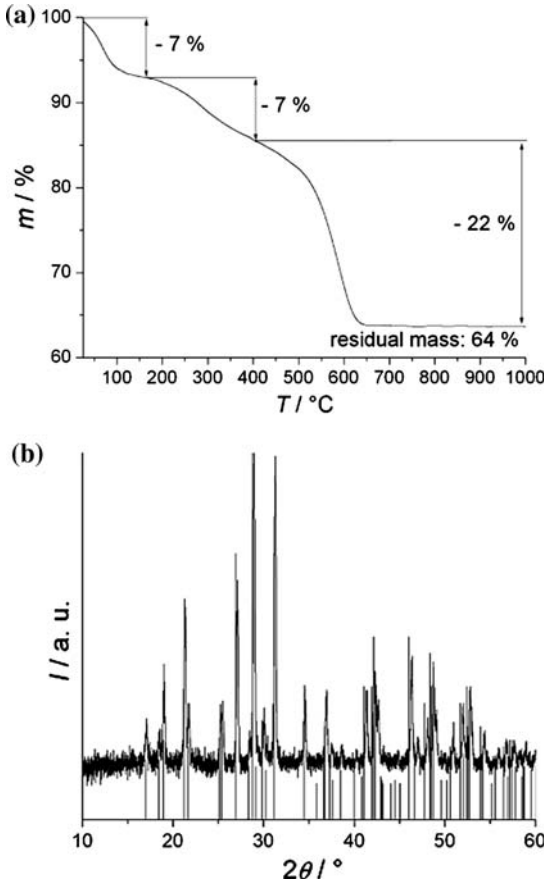

Fig. 10 **a** TG curve of NC-DEG measured in a flow of air. **b** XRD pattern taken on the residue after TG; a pattern of monazite is represented as line diagram (PDF card 32-199)

Fig. 11 Representative ring specimens before and after ring upsetting tests shown in the order: **a** before test, **b** without lubricant, **c** with NC-DEG, **d** with CMK-3, and **e** with reference lubricant

the dimensionless friction factor, m [29, 30]. A flat ring specimen is plastically compressed between two coplanar upsetting plates under dry friction conditions (no lubricant) or in the presence of a lubricant. From the reduction of the inner diameter, d_i, of the ring, which is associated with the occurring friction during compression, m can be determined (see "Experimental section" for details). The smaller the d_i after compression—the larger the reduced inner diameter d_{iRed}—the stronger the frictional forces that had occurred during compression. Large values of d_{iRed} and m indicate high friction (poor lubrication).

In our ring upsetting tests, a specimen made of a non-alloy carbon steel with $d_i = 15$ mm (Fig. 11) was used. The tests were performed in air at 750 °C (typical conditions in warm forming processes) in the presence of CMK-3, NC-DEG, and a commercial grade graphite-based lubricant as well as in the absence of any lubricant. The two latter conditions served as references for the evaluation. Among our three nanocomposite materials, only the NC-DEP was chosen for the tests because it contained the largest fraction of nanocrystals and was most simply synthesized. A rather large amount of material per ring upsetting test is needed, and synthesis of such large amounts of carbons and nanocomposites still poses a problem.

Figure 11 displays photographs of the specimen after the ring upsetting tests, and Table 1 summarizes the values obtained for d_{iRed} and m. It can be seen on the photographs that d_i strongly increased in the order—no lubricant, NC-DEG, CMK-3 and graphite-based lubricant—revealing

Table 1 Inner diameter (d_i) and reduced inner diameter (d_{iRed}) of the specimen after the ring upsetting tests and obtained friction factors (m)

Condition	d_i (mm)	d_{iRed} (%)	m
No lubricant	6	59	1.8[a]
NP-DEG	9	40	0.8
CMK-3	10	33	0.6
Graphic-based lubricant	14	10	0.2

[a] The value of m is outside the range of definition ($0 \leq m \leq 1$) indicating that very strong frictional forces occurred, and that the friction factor model was not valid here

that friction was dramatically lowered in the same order. This was expected for the two reference conditions but, in addition, indicated that both CMK-3 and NC-DEG exhibited some lubrication properties. The observed trend is quantified by values of *m*. For CMK-3 and NC-DEP, these values are 3–4 times, respectively, larger than for the graphite-based lubricant meaning that they are 3–4 times, respectively, less efficient in lowering frictional forces than the reference lubricant. On the contrary, their values of *m* are significantly smaller than for the dry friction condition. Interestingly, the fact that *m* is only slightly larger for NC-DEG than for CMK-3 suggests that the nanocrystals do not have a very pronounced influence on the lubrication properties of the carbon material, possibly because of their small size. One would expect that the presence of the nanocrystals, due to their hard ceramic nature, should result in a significant reduction of the lubrication properties of the nanocomposites compared to the pure carbon material. Taken together, the figures are not spectacular, yet, appear promising, in particular when considering that there obviously exists great potential for the improvement of the lubrication properties of the CMK-3 and nanocomposites by transforming the amorphous structures of the carbon walls into graphitic structures. No efforts had been made here in that direction.

Conclusions

We have shown for the first time that composites of an OMC and metal phosphate nanocrystals can be successfully prepared. With new potential applications of OMC-based nanocomposites in forging processes in mind, three different CMK-3/$CePO_4$:Tb nanocomposite materials were synthesized. In two cases, the pores were evidently loaded with $CePO_4$:Tb nanocrystals; in one case, however, most nanocrystals merely adhered to the outer surfaces of the carbon particles. The residues after combustion exhibited upon excitation with UV light the typical green luminescence of Tb^{3+}. We have performed a preliminary evaluation of the lubrication properties of the CMK-3 and one CMK-3/$CePO_4$:Tb nanocomposite material. The friction factors determined by means of ring upsetting tests revealed that the carbon materials were able to lower frictional forces although they were 3–4 times less efficient than a commercial graphite-based reference lubricant. Our results, nevertheless, indicate that the OMC-based nanocomposites have potential for further development as advanced lubrication systems that integrate functional species. Further work will be directed to the improvement of the lubrication properties by transforming the amorphous structures of the carbon walls into graphitic structures, the up-scaling of the synthesis routes to produce larger amounts of material (for example, by changing from nanocasting to self-assembly methods [4]), and testing the performance of the incorporated fluorescent nanocrystals for optical quality checks of workpieces and tools in forging processes.

References

1. Ryoo R, Joo SH, Jun S (1999) J Phys Chem B 103:7743
2. Lee J, Kim J, Hyeon T (2006) Adv Mater 18:2073
3. Lu A-H, Schüth F (2006) Adv Mater 18:1793
4. Wan Y, Shi Y, Zhao D (2008) Chem Mater 20:932
5. Liang C, Li Z, Dai S (2008) Angew Chem Int Ed 47:3696
6. Stein A, Wang Z, Fierke MA (2009) Adv Mater 21:265
7. Kim TW, Park IS, Ryoo R (2003) Angew Chem Int Ed 42:4375
8. Yang H, Yan Y, Liu Y, Zhang F, Zhang R, Meng Y, Li M, Xie S, Tu B, Zhao D (2004) J Phys Chem B 108:17320
9. Kim CH, Lee D-K, Pinnavaia TJ (2004) Langmuir 20:5157
10. Lee KT, Ji X, Rault M, Nazar LF (2009) Angew Chem Int Ed 48:1
11. Jun Y-S, Hong WH, Antonietti M, Thomas A (2009) Adv Mater 21:1
12. Joo SH, Choi SJ, Oh I, Kwak J, Liu Z, Terasaki O, Ryoo R (2001) Nature 412:169
13. Fan J, Wang T, Yu C, Tu B, Jiang Z, Zhao D (2004) Adv Mater 16:1432
14. Dong X, Shen W, Gu J, Xiong L, Zhu Y, Li H, Shi J (2006) J Phys Chem B 110:6015
15. Lu A-H, Li W-C, Hou Z, Schüth F (2007) Chem Commun 1038
16. Zhu S, Zhou H, Hibino M, Honma I, Ichihara M (2005) Adv Funct Mater 15:381
17. Huwe H, Fröba M (2007) Carbon 45:304
18. Fulvio PF, Jaroniec M, Liang C, Dai S (2008) J Phys Chem C 112:13136
19. Jung S, Joo SH, Ryoo R, Kruk M, Jaroniec M, Liu Z, Ohsuma T, Terasaki O (2000) J Am Chem Soc 122:10712
20. Lee J-S, Joo SH, Ryoo R (2002) J Am Chem Soc 124:1156
21. Solovyov LA, Shmakov AN, Zaikovski VI, Joo SH, Ryoo R (2002) Carbon 40:2477
22. Fuertes AB (2004) Microporous Mesoporous Mater 67:273
23. Gierszal KP, Kim T-W, Ryoo R, Jaroniec M (2005) J Phys Chem B 109:23263
24. Lehmann O, Meyssamy H, Kömpe K, Schnablegger H, Haase M (2003) J Phys Chem B 107:7449
25. Kömpe K, Lehmann O, Haase M (2006) Chem Mater 18:4442
26. Buissette V, Moreau M, Gascoin T, Boilot J-P, Chane-Ching J-Y, Le Mercier T (2004) Chem Mater 16:3767
27. Feldmann C, Jungk H-O (2002) J Mater Sci 37:3251. doi: 10.1023/A:1016131016637
28. Feldmann C (2003) Adv Funct Mater 13:101
29. Sofuoglu H, Rasty J (1999) Tribol Int 32:327
30. Sofuoglu H, Gediki H, Rasty J (2001) ASLE Trans 123:338
31. Tiemann M (2008) Chem Mater 20:961
32. Riwotzki K, Meyssamy H, Schnableger H, Kornowski A, Haase M (2001) Angew Chem Int Ed 40:573
33. Li Q, Yam VW-W (2007) Angew Chem Int Ed 46:3486